Journal of Materials Chemistry C

ROYAL SOCIETY OF CHEMISTRY

PAPER

View Article Online
View Journal | View Issue

Check for updates

Cite this: J. Mater. Chem. C, 2022, 10, 11719

Decisive role of heavy-atom orientation for efficient enhancement of spin–orbit coupling in organic thermally activated delayed fluorescence emitters†

Michał Mońka,[a] Daria Grzywacz,[b] Estera Hoffman,[a] Vladyslav Ievtukhov,[b] Karol Kozakiewicz,[b] Radoslaw Rogowski,[a] Aleksander Kubicki,[a] Beata Liberek,[b] Piotr Bojarski[a] and Illia E. Serdiuk *[a]

In view of the rapidly growing interest in the hybrid materials for heavy-metal-free optoelectronics, the research described here aimed to confirm the potential ability of abundant heavy atoms (HAs) in improving key parameters of organic emitters with thermally activated delayed fluorescence. Namely, the enhancement of reverse intersystem crossing (rISC) while keeping a reasonable value of fluorescence rate was investigated in red emitters with bromine atom(s) introduced into the ortho positions of the *N*,*N*-ditolylaniline donor fragment. The results of photophysical investigations and quantum chemical calculations indicate that selective acceleration of rISC by HAs without a substantial decrease of the fluorescence rate is possible. Molecular design principles of such hybrid materials, however, do not seem simple. In the investigated emitters, the oscillator strength of the S_1–S_0 transition which defines the fluorescence rate is not directly influenced by the bromine atoms, and remains similar or decreases weakly for the brominated emitters. The maximal enhancement of spin–orbit coupling (SOC) does not depend directly on the number of HAs either, but on their relative position and orientation in the emitter. The analysis of numerous rotational isomers of emitters revealed that SOC enhancement cannot be explained by either the internal or the external HA effect. Taking into account the lack of significant contribution of bromines in orbital and spin momentum of the T_1–S_1 transition, but yet significant SOC enhancement, we explain the observed phenomenon as a heavy-atom field effect (HAFE) which increases the total angular momentum. The most impressive SOC enhancement by the HAFE up to 60 times is observed when HAs align asymmetrically and are oriented towards the chromophore fragment with the largest orbital momentum change. Another important observation reveals that, in the case of symmetrical structures, the field of a heavy atom can be compensated by another one leading to almost zero SOC and 650-fold rISC inhibition. Such species should be avoided at the stage of molecular design planning.

Received 26th April 2022,
Accepted 5th July 2022

DOI: 10.1039/d2tc01729f

rsc.li/materials-c

Open Access Article. Published on 01 August 2022. Downloaded on 2/7/2026 9:48:07 AM.
This article is licensed under a Creative Commons Attribution 3.0 Unported Licence.

Introduction

Hybrid organic emitters bearing cheap and abundant non-metallic heavy atoms (HAs) attract more and more attention lately.[1–4] Such materials can be the Golden mean between all-organic materials and heavy-metal complexes or inorganic analogues. Potentially, the rational design of such hybrid materials can preserve the advantages of organic and heavy-metal materials to enable fast conversion of electric energy into light in a submicrosecond regime but avoid low efficiency of organics and high cost and environmental issues connected with the use of heavy metals.

Nowadays, the application of various emitters in organic light emitting diodes (OLEDs) is realized *via* two main strategies which represent separate solutions for the problem of triplet harvesting under electric excitation. Widely commercialized generation of phosphorescent heavy-metal complexes converts all the electrically generated excitons to the triplet ones.[5] Due to very high values of spin–orbit coupling (SOC) of the T_1–S_0 transition caused by the presence of a heavy-metal, such excitons are deactivated radiatively within 1–10 μs.

[a] Faculty of Mathematics, Physics and Informatics, University of Gdańsk, Wita Stwosza 57, 80-308 Gdańsk, Poland. E-mail: illia.serdiuk@ug.edu.pl; Tel: +48 58 523 22 44
[b] Faculty of Chemistry, University of Gdańsk, Wita Stwosza 63, 80-308 Gdańsk, Poland

† Electronic supplementary information (ESI) available: additional results of photophysical investigations, computationally predicted electronic parameters and calculated rISC rate constants for various rotamers, NMR spectra. See DOI: https://doi.org/10.1039/d2tc01729f

Open Access Article. Published on 01 August 2022. Downloaded on 2/7/2026 9:48:07 AM.
This article is licensed under a Creative Commons Attribution 3.0 Unported Licence.

Recently, various attempts were made to substitute such heavy-metal materials with organic analogues for application in such phosphorescence OLEDs.[6–8] However, the best pure organic candidates phosphoresce in the second or millisecond time domain and/or with low quantum yields.[9–11] Very recent approaches of incorporation of abundant non-metallic heavy atoms like selenium in organic materials provide submillisecond phosphorescence (385 μs) with a 20% quantum yield.[6] These data indicate that we are still far away from efficient organic phosphors.

The second strategy for OLED emitters expected to be closer to commercialization utilizes the thermally activated delayed fluorescence (TADF) phenomenon.[12] In TADF materials, the radiative deactivation of all excitons occurs from the singlet S_1 state. Conversion of triplet excitons to singlet ones occurs *via* endothermic spin–flip transition named reverse intersystem crossing (rISC). It is enabled by the energetic proximity of the lowest excited singlet and triplet states in TADF emitters. Being "spin–forbidden", rISC still depends on SOC. However, in contrast to the all-organic phosphorescent materials, some of their TADF analogues are capable of 100% quantum yields of luminescence within micro- and submicrosecond regimes.[13] Taking into account the most recent achievements,[14–17] development of organic and hybrid TADF materials seems to be the most promising direction for environment friendly multifunctional optoelectronics.

One of the most critical problems of organic TADF materials remains the slow rate of triplet harvesting.[18,19] Acceleration of rISC while maintaining the fast fluorescence rate is supposed to be a solution for the minimization of the external quantum efficiency (EQE) roll-off under increasing current density and low stability of OLED devices in general. In light-atom organic materials due to weak SOC, efficient rISC can be achieved mainly *via* minimization of the energy gap between the S_1 and T_1 states (ΔE_{ST}): the lower the ΔE_{ST} value, the higher the rate constant of rISC (k_{rISC}). In general, small ΔE_{ST} requires strong spatial separation of the highest occupied (HOMO) and the lowest unoccupied molecular orbital (LUMO). For this reason an overwhelming number of TADF emitters are strong electron donor–acceptor (D–A) molecular systems whose S_1 and T_1 states have charge-transfer (CT) nature with a high transition dipole moment.

Another important parameter of a TADF emitter is its emissive rate. In donor–acceptor emitters, the latter is proportional to the oscillator strength of the ^{1}CT-S_0 transition ($f_{1CT\text{-}S0}$). The above mentioned separation of HOMO and LUMO unavoidably leads to the decrease of $f_{1CT\text{-}S0}$, or in terms of selection rules, the ^{1}CT-S_0 transition becomes forbidden. Low oscillator strength is clearly a negative factor for an OLED emitter, which elongates the conversion of excitation energy to light. Taking this into account, the relation of key parameters of D–A type TADF emitters can be expressed as:

$$f_{1CT\text{-}S0} \sim 1/k_{rISC}. \quad (1)$$

Within the light-atom organic D–A materials, a solution to this dilemma is extremely challenging, because most of the structural changes sacrifice either the rISC rate and thus triplet harvesting efficiency or the ^{1}CT-state radiative deactivation rate constant (k_r) and thus fluorescence efficiency (Fig. 1). Fastly evolving hybrid materials based on organic emitters modified with HAs can potentially solve this dilemma. As correlation (1) is caused by different indirect electronic reasons, the presence of HAs can increase SOC, but hypothetically should not affect the fluorescence rate. However, in spite of the rapidly growing interest in such materials,[14–17] very scarce knowledge on the mechanism of HA action on organic TADF emitters prevents their targeted rational molecular design. Taking into account the complex nature of TADF, the effect of a particular heavy atom on the nature of electronic states and other parameters connected with $f_{1CT\text{-}S0}(k_r)$ and k_{rISC}(SOC) is highly unintuitive and should be extensively investigated.

In this research, we aimed to find a molecular strategy for the HA-modification of an organic TADF emitter so that it could preserve its fluorescence rate but enhance the rISC rate. The most suitable molecular design strategy for such modifications seems to be the one compromising the ΔE_{ST} and $f_{1CT\text{-}S0}$ values as reported recently.[20] This strategy relies on a smaller separation of HOMO and LUMO in red and NIR emitters with a highly

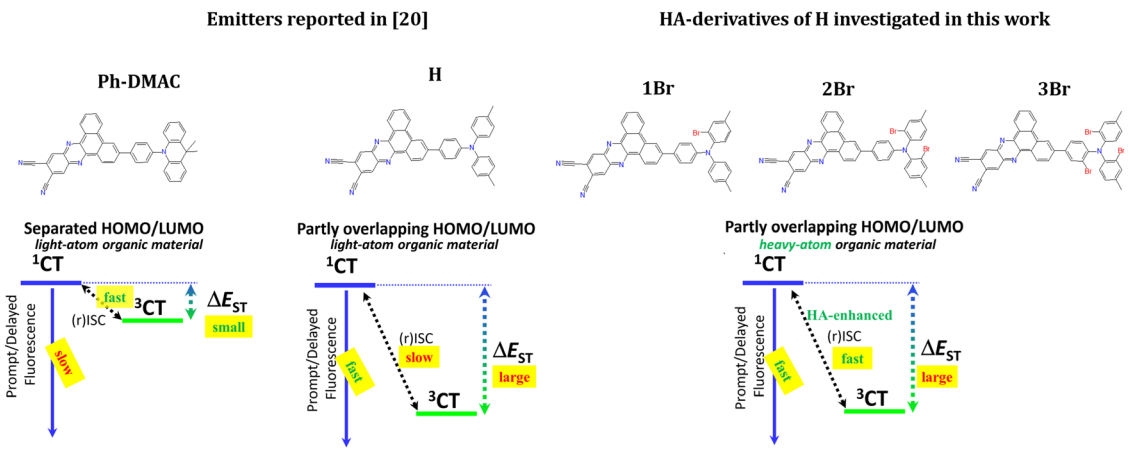

Fig. 1 Canonic structures of the investigated emitters with a schematic representation of excited states and key processes leading to light emission.

 This journal is © The Royal Society of Chemistry 2022

Open Access Article. Published on 01 August 2022. Downloaded on 2/7/2026 9:48:07 AM.
This article is licensed under a Creative Commons Attribution 3.0 Unported Licence.

stabilized CT state. It utilizes a partly conjugated donor with a strong acceptor fragment[20,21] and sacrifices the reduction of ΔE_{ST} for a higher $f_{1CT\text{-}S0}$ value. The thus developed 11,12-dicyanodibenzo[*a*,*c*]phenazine emitter bearing a more planar *N*,*N*-ditolylaniline (DTA) donor (emitter **H**, Fig. 1) in comparison with a highly twisted 10-phenyl-9,9-dimethylacridan (**Ph-DMAC**) donor was reported to have a 12 times higher k_r value. Simultaneously, the ΔE_{ST} increased almost 3.7 times causing a 30-fold drop in k_{rISC}. The authors also performed OLED tests, which confirmed that in spite of k_r increase, rISC inhibition led to worse device work due to a much higher EQE roll-off. One should also note that the described emitters are one of the best representatives of red/NIR TADF emitters,[22] and thus their further improvement seems to be very topical for OLED technology.

Taking into account the good fluorescent properties but unsatisfactory slow rISC, in this work, **H** was modified with heavy atoms. Bromine was selected as HAs thanks to its abundance, low cost and easiness of introduction into organic molecules. Next, possible positions of HAs in the emitter's structure were analyzed. According to our previous findings,[23] one should avoid direct electronic interaction of HAs with the fragment responsible for the lowest excited triplet state of local character (^{3}LE) to avoid intersystem crossing (ISC) enhancement *via* the ^{1}CT→^{3}LE(HA) channel, which is a negative factor regarding triplet harvesting efficiency. The reported phosphorescence investigations indicate that a triplet state localized on a triarylamino donor fragment has energy near 3.05 eV.[24] Triplet energy of dibenzo[*a*,*c*]phenazine acceptor derivatives is below 2.50 eV,[25] which makes it the lowest ^{3}LE state in such kinds of emitters. For these reasons, one, two, and three bromine atoms were introduced into the donor, namely, at the *ortho* position of each of the benzene rings of the DTA fragment, providing emitters **1Br**, **2Br**, and **3Br**, respectively (Fig. 1). Thorough analysis of the photophysical properties with the help of DFT calculations allowed us to reveal and explain rISC enhancement whilst maintaining a reasonable k_r value. In the example of red TADF emitters, it was found that HAs in *ortho* positions of triarylamine donors enrich rotational isomerism of emitting species. The analysis of electronic features of such rotamers afforded valuable conclusions on the effect of relative positions of HAs on spin–orbit coupling and rISC.

Synthesis

3-(4-(Di-*p*-tolylamino)phenyl)dibenzo[*a*,*c*]phenazine-11,12-dicarbonitrile (**H**) was synthesized by the reaction of 3-(4-(di-*p*-tolylamino)phenyl)phenanthrene-9,10-dione (**1**) with 4,5-diaminophthalonitrile (Scheme 1), conducted according to the procedure described in the literature.[20] Bromination of **H** with 1.1 eq. of NBS gave **1Br**. Analogous bromination of **H** with 2.1 and 3.1 eq. of NBS was less selective. Therefore, we decided to brominate first substrate **1** with 2.1 and 3.1 eq. of NBS, which gave us **2** and **3**, respectively. Finally, **2Br** and **3Br** were obtained by cyclization of **2** and **3** with 4,5-diaminophthalonitrile.

Experimental section

Generals

Zeonex® (ZNX, Zeonex480R, density = 1.01 g cm^{-3}), 4,4′-bis(*N*-carbazolyl)-1,1′-biphenyl (CBP, sublimated), reagents for synthesis, and solvents of respective grades for spectroscopy and synthesis were purchased and used without further purification.

Synthesis and analysis

The ^{1}H NMR spectra were recorded on a Bruker AVANCE III 500 (500.13/125.76 MHz) instrument, under standard experimental conditions in $CDCl_3$ with internal Me_4Si. The ^{13}C NMR spectra were unavailable due to the low solubility of the investigated compounds. Positive-ion mode MALDITOF mass spectra were obtained using a Bruker Biflex III spectrometer with 2,5-dihydroxybenzoic acid matrixes. Purification by column chromatography was performed on silica gel (70–230 mesh).

3-(4-(Di-*p*-tolylamino)phenyl)phenanthrene-9,10-dione (**1**) and 3-(4-(di-*p*-tolylamino)phenyl)dibenzo[*a*,*c*]phenazine-11,12-dicarbonitrile (**H**) were obtained according to the procedures described in the literature.[20]

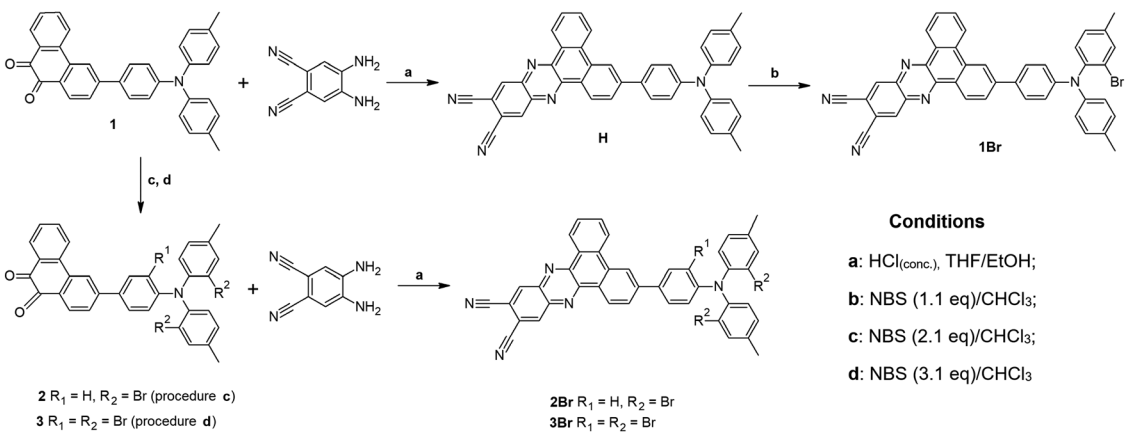

Scheme 1 Synthetic scheme for the investigated emitters.

Open Access Article. Published on 01 August 2022. Downloaded on 2/7/2026 9:48:07 AM.
This article is licensed under a Creative Commons Attribution 3.0 Unported Licence.

General procedure for bromination of 1 and H

NBS (1.1 eq., 2.1 eq., or 3.1 eq., respectively) was added to **1** or **H** and dissolved in $CHCl_3$ (8 mL). After stirring overnight at rt in the absence of light, the solution was concentrated and MeOH (5 mL) was added to the residue. The precipitated solid was filtered, washed and purified by silica gel column chromatography (eluent: $CHCl_3$/*n*-hexane 1/5).

3-(4-(Bis(2-bromo-4-methylphenyl)amino)phenyl)phenanthrene-9,10-dione (2)

Bromination of **1** (60 mg, 0.13 mmol) with 2.1 eq. of NBS (49 mg, 0.27 mmol) gave **2** (red solid, 70 mg, 84%). ^{1}H NMR (500 MHz, $CDCl_3$-*d*): δ ppm 2.36 (s, 6 H), 6.71 (d, J = 8.85 Hz, 2 H), 7.12 (dd, J= 7.93, 0.61 Hz, 2 H), 7.19 (d, J = 7.93 Hz, 2 H), 7.48 (td, J = 7.62, 0.61 Hz, 1 H), 7.50 (d, J = 1.53 Hz, 2 H), 7.56 (dt, J = 8.85, 2.14 Hz, 2 H), 7.65 (dd, J = 8.24, 1.53 Hz, 1 H), 7.72 (td, J = 7.33, 1.53 Hz, 1 H), 8.10 (d, J = 7.93 Hz, 1 H), 8.18 (d, J = 1.53 Hz, 1 H), 8.21 (dd, J = 7.93, 1.53 Hz, 1 H), 8.22 (d, J = 8.24 Hz, 1 H); MALDITOF-MS: *m*/*z*: calcd for $C_{34}H_{23}Br_2NO_2$ 637.2, found 638.0 $[M + 1]^+$.

3-(4-(Bis(2-bromo-4-methylphenyl)amino)-3-bromophenyl)-phenanthrene-9,10-dione (3)

Bromination of **1** (60 mg, 0.13 mmol) with 3.1 eq. of NBS (70 mg, 0.40 mmol) gave **3** (orange solid, 79 mg, 85%). ^{1}H NMR (500 MHz, $CDCl_3$-*d*): δ ppm 2.34 (s, 6 H), 6.77 (d, J = 8.54 Hz, 1 H), 6.80 (d, J = 8.24 Hz, 1 H), 6.93 (d, J = 8.24 Hz, 1 H), 7.05 (2 × d, J = 7.93 Hz, 2 H), 7.45 (2 × s, 2 H), 7.51 (t, J = 7.63/7.33 Hz, 1 H), 7.52 (dd, J = 8.24 Hz, J = 2.14 Hz, 1 H), 7.64 (d, J = 8.24 Hz, 1 H), 7.75 (t, J = 7.63/7.47 Hz, 1 H), 7.93 (d, J = 2.14 Hz, 1 H), 8.12 (d, J = 8.24 Hz, 1 H), 8.17 (s, 1 H), 8.22 (d, J = 7.63 Hz, 1 H), 8.25 (d, J = 7.94 Hz, 1 H); MALDITOF-MS: *m*/*z*: calcd for $C_{34}H_{22}Br_3NO_2$ 715.2, found 716.1 $[M + 1]^+$.

3-(4-((2-Bromo-4-methylphenyl)(p-tolyl)amino)phenyl)dibenzo[a,c]phenazine-11,12-dicarbonitrile (1Br)

Bromination of **H** (42 mg, 0.07 mmol) with 1.1 eq. of NBS (14 mg, 0.08 mmol) led to **1Br** (red solid, 40 mg, 84%). ^{1}H NMR (500 MHz, $CDCl_3$-*d*): δ ppm 2.35–2.40 (4 × s, 6 H), 7.03 (d, J = 8.85 Hz, 1 H), 7.05–7.15 (m, 5 H), 7.17–7.23 (m, 2 H), 7.52 (dd, J = 10.38, 1.83 Hz, 1 H), 7.67 (d, J = 8.54 Hz, 1 H); 7.68 (d, J = 8.85 Hz, 1 H); 7.80 (tdd, J = 7.94, 2.75, 1.53 Hz, 1 H), 7.91 (tdd, J = 7.63, 2.75, 1.53 Hz, 1 H), 7.98 (dt, J = 8.54, 1.53 Hz, 1 H), 8.64 (dd, J = 8.09, 3.36 Hz, 1 H), 8.71 (bs, 1 H), 8.76 (dd, J = 1.83, 0.61 Hz, 1 H); 8.77 (t, J = 0.61 Hz, 1 H); 9.32 (dd, J = 8.24, 3.66 Hz, 1 H), 9.34 (dt, J = 8.24, 1.52 Hz, 1 H); MALDITOF-MS: *m*/*z*: calcd for $C_{42}H_{26}Br_1N_5$ 679.2, found 680.2 $[M + 1]^+$.

General procedure for the synthesis of 2Br and 3Br

4,5-Diaminophthalonitrile (1.2 eq.) was added to **2** or **3** and dissolved in THF/EtOH (1 : 1; 5 mL) with $HCl_{(conc)}$ (10 μL). After stirring overnight at rt the solution was concentrated and purified by silica gel column chromatography (eluent: $CHCl_3$/*n*-hexane 1/3).

3-(4-(Bis(2-bromo-4-methylphenyl)amino)phenyl)dibenzo[*a*,*c*]phenazine-11,12-dicarbonitrile (2Br)

Reaction of 4,5-diaminophthalonitrile (12 mg, 0.076 mmol) with **2** (40 mg, 0.063 mmol) gave **2Br** (red solid, 40 mg, 83%). ^{1}H NMR (500 MHz, $CDCl_3$-*d*); 2.37 (s, 6 H), 6.79 (dt, J = 8.85, 2.14 Hz, 2 H), 7.13 (ddd, J= 8.24, 2.14, 0.61 Hz, 2 H), 7.19 (d, J = 8.24 Hz, 2 H), 7.51 (dd, J = 1.83, 0.61 Hz, 2 H), 7.69 (dt, J = 8.85, 2.14 Hz, 2 H), 7.80 (td, J= 7.02, 2.14 Hz, 1 H), 7.91 (td, J= 7.32, 1.53 Hz, 1 H), 7.99 (dd, J = 8.54, 1.53 Hz, 1 H), 8.65 (d, J= 7.94 Hz, 1 H), 8.73 (d, J = 1.53 Hz, 1 H), 8.79 (dd, J= 3.66, 0.61 Hz, 2 H), 9.33 (d, J = 8.24 Hz, 1 H), 9.36 (dd, J = 7.93, 1.53 Hz, 1 H); MALDITOF-MS: *m*/*z* calcd for $C_{42}H_{25}Br_2N_5$ 759.2, found 759.2 $[M]^+$.

Synthesis of 3-(4-(bis(2-bromo-4-methylphenyl)amino)phenyl) dibenzo[*a*,*c*]phenazine-11,12-dicarbo-nitrile (3Br)

Reaction of 4,5-diaminophthalonitrile (10 mg, 0.067 mmol) with **3** (40 mg, 0.056 mmol) gave **3Br** (yellow solid, 38 mg, 81%). ^{1}H NMR (500 MHz, $CDCl_3$-*d*); 2.37 (s, 6 H), 6.83 (d, J = 8.24 Hz, 1 H), 6.87 (d, J = 7.96 Hz, 1 H), 7.01 (d, J = 8.24 Hz, 1 H), 7.09 (dd, J = 7.96 Hz, J = 1.37 Hz, 2 H), 7.49 (bs, 2 H), 7.68 (dd, J = 8.51, 2.20 Hz, 1 H), 7.85 (t, J = 7.69 Hz, 1 H), 7.96 (ddd, J = 8.51 Hz, J = 7.14 Hz, J = 1.37 Hz, 1 H), 8.00 (dd, J = 8.51, 1.65 Hz, 1 H), 8.09 (d, J = 1.92 Hz, 1 H), 8.69 (d, J = 8.24 Hz, 1 H), 8.74 (d, J = 1.37 Hz, 1 H), 8.82 (d, J = 1.1 Hz, 1 H), 8.82 (m, 1 H), 9.38 (dd, J = 7.96 Hz, J = 1.1 Hz, 1 H), 9.39 (d, J = 8.51 Hz, 1 H); MALDITOF-MS: *m*/*z*: calcd for $C_{42}H_{24}Br_3N_5$ 837.2, found 838.1 $[M + 1]^+$.

The NMR spectra of the obtained compounds can be found in the ESI.†

Sample preparation for photophysical measurements

Films in ZNX and CBP were prepared by the spin-coating method; the final mass fractions of dispersed emitters were *ca.* 0.1% and 6%, 10%.

Photoluminescence measurements

UV-Vis absorption spectra were recorded using a Shimadzu UV-1900 spectrophotometer. Steady-state photoluminescence spectra were recorded using an FS5 spectrofluorometer (Edinburgh Instruments) using front-face excitation geometry. Absolute PL quantum yields (PLQYs) were measured using an integrating sphere (Quantaurus C11347-11, Hamamatsu). Time-resolved measurements were performed at different temperatures using a customized system[26] consisting of a pulsed YAG:Nd laser (PL2251A, EKSPLA) coupled with an optical parametric generator (PG 401/SH) as the excitation light source and 2501S grating spectrometer (Bruker Optics) combined with a streak camera system (C4334-01 Hamamatsu) as the detection unit. The system was equipped with a double-stage high vacuum pump (T-Station 85 Edwards) coupled with a closed-cycle helium cryostat (APD DE-202) and a temperature controller (LakeShore 336). To reduce scattering, reflections and secondary order artifacts, a set of various high performance optical bandpass (BP) and longpass (LP) filters were used, in the excitation path 325/50BP or 375/50BP (CWL/FWHM), depending on the selected excitation wavelength, together with

 This journal is © The Royal Society of Chemistry 2022

Open Access Article. Published on 01 August 2022. Downloaded on 2/7/2026 9:48:07 AM.
This article is licensed under a Creative Commons Attribution 3.0 Unported Licence.

LP filters: 375LP or 350LP (Edmund Optics). In order to build PL intensity decay profiles, streak camera images were integrated over a constant specified wavelength interval. Radiative rate constants k_r and (reverse) intersystem crossing rates $k_{(r)ISC}$ were calculated using procedures described in detail previously and in Section S4 (ESI†).[23]

Quantum chemical calculations

Quantum chemical calculations were conducted at the DFT/TD-DFT level of theory using the Gaussian 16 program package.[27] The B3LYP functional was used with the LAN2LDZ basis set.[28] Unspecific solvent effect (toluene) was included at the level of the Polarized Continuum Model (PCM).

First, for each compound, unconstrained geometry optimizations were performed for the ground (S_0), excited singlet (S_1) and excited triplet electronic (T_1, T_2) states. Convergence of all geometry optimizations was verified by the vibrational analysis, and no negative frequencies were observed; therefore, the calculated minima correspond to "true" stationary points. The nature of electronically excited states was determined by the analysis of molecular orbitals. Spin–orbit coupling constants were computed using the ORCA 4.2 software package[29] with B3LYP functional and DEF2-TZVP basis set with included relativistic zero-order regular approximation (ZORA).

Results and discussion

Absorption spectra

The effect of bromine substitution on the ground state (S_0) of emitters can be analyzed from the absorption spectra (Fig. 2A). In solutions, the long wavelength absorption maximum responsible for the S_0–^{1}CT transition shifts gradually to higher energies with the number of introduced bromines. There are two main factors which can cause such an effect: (*i*) the electron-withdrawing feature of bromine as a halogen, which reduces the donor strength and thus increases the energy of the CT state and (*ii*) the increase of the dihedral angle between the donor and acceptor fragment due to the large size of bromine atoms in the *ortho* position, leading to further HOMO–LUMO separation and reduction of conjugation between molecular fragments. The important consequence of the *ii* factor is the decrease of oscillator strength f_{S0-1CT}. This is not the case for **1Br** and **2Br**, as determined oscillator strength is almost equal or increases as compared to **H** (Table 1).

This indicates that the electron-withdrawing feature of bromine has a key influence on the CT absorption band. Compound **3Br** exhibits the highest blue shift together with an imaginary increase of the *f* value. The latter is explained by a

Table 1 Absorption parameters for dichloromethane solutions of emitters

Cmpd	λ_{abs} [nm]	f_{S0-1CT} Experimental	f_{S0-1CT} Calculated[a]
H	502	0.214	0.107
1Br	483	0.206	0.131
2Br	474	0.289	0.216
3Br	435	0.450	0.118

[a] Calculated f_{S0-1CT} is a statistical mean value for various rotamers discussed further; calculated by taking into account the probability of each rotamer predicted by Boltzmann distribution at 298 K.

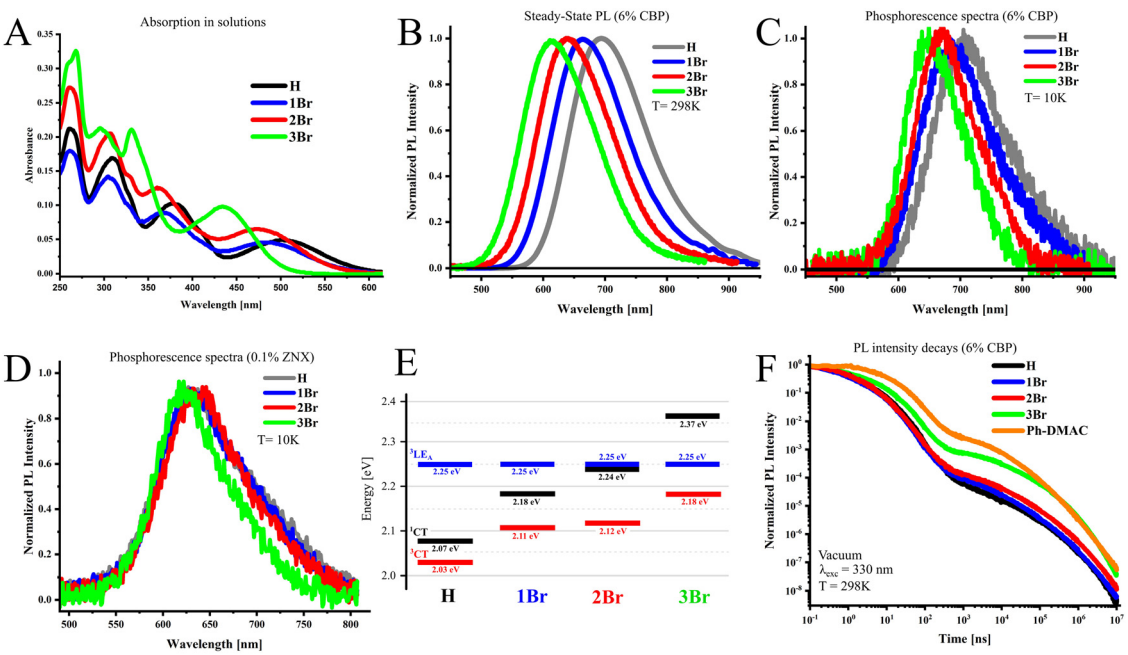

Fig. 2 Absorption spectra in dichloromethane solutions (A); steady-state PL spectra of the investigated compounds in 6% CBP measured under excitation wavelength λ_{exc} = 330 nm (B); phosphorescence spectra in 6% CBP (T = 10 K, 20 ms delay after excitation pulse) (C); phosphorescence spectra in 0.1% ZNX (T = 10 K, 20 ms delay) (D); alignment of excited states in respective compounds determined from steady-state PL and phosphorescence onsets (E); and PL intensity decays of the investigated compounds in 6% CBP (F).

Open Access Article. Published on 01 August 2022. Downloaded on 2/7/2026 9:48:07 AM.
This article is licensed under a Creative Commons Attribution 3.0 Unported Licence.

strong overlap of the CT absorption with the next band near 400 nm, which disables experimental determination of f_{S0-1CT}. As discussed further, DFT calculations confirm close f_{S0-1CT} values for all compounds.

Photoluminescence spectra and alignment of excited states

The photoluminescence (PL) features of emitters were investigated in the amorphous film media, namely, 4,4′-bis(*N*-carbazolyl)-1,1′-biphenyl (CBP), widely used as a host material for OLEDs. In CBP films, the PL maximum of the investigated emitters shifts from red-NIR to orange-red with the increasing number of bromine atoms in the donor fragment (Fig. 2B, Table 2). In 6% w/w films, according to the PL onset values (Fig. S1A, ESI†), the ^{1}CT state energy increases from 2.07 eV in **H** by 0.11 eV (**1Br**, 2.18 eV) and by 0.17 eV (**2Br**, 2.24 eV), when the first and second bromine atoms are introduced into the side phenyl rings (Table S1, ESI†). Similarly to absorption, the appearance of third bromine in the linker phenyl ring (**3Br**) causes the strongest ^{1}CT-energy increase by 0.30 eV, reaching 2.37 eV. PL quantum yields vary from moderate high 61% in **3Br** to almost absolute in **2Br**. The phosphorescence spectra measured at 10 K with a 20 ms delay after the excitation pulse exhibit similar dependence, but the absolute shifts are smaller (Fig. 2C, Table 2). The energy of the ^{3}CT-state derived from phosphorescence onsets (Fig. S1B, ESI†) increases thus by 0.06 eV (**1Br**), 0.08 eV (**2Br**), and 0.13 eV (**3Br**) compared to **H**. The described spectral measurements indicate that ΔE_{ST} increases from 0.04 eV in **H** to 0.08 eV (**1Br**) and 0.13 eV (**2Br**) and reaches maximal 0.20 eV for **3Br**. At a higher doping concentration (10%), spectral behavior is generally similar (Fig. S1C and D, ESI†); however, PL spectra shift 5–10 nm to the red which results in a slight decrease of ΔE_{ST} by 10–30 meV (Table S1, ESI†).

To estimate the energy of the higher triplet state, phosphorescence measurements were performed in nonpolar Zeonex® (ZNX) polymer, where the CT states are destabilized. In ZNX films, the phosphorescence onset is almost identical for all emitters and provides the energy of a triplet state near 2.25 eV (Fig. 2D and Fig. S2, ESI†). Under such conditions, phosphorescence most likely occurs from the triplet state with a dominating locally-excited character (^{3}LE). As substitution in the donor does not affect its energy, such a ^{3}LE-state is localized on the acceptor fragment identical to all emitters, which is supported by the phosphorescence spectra of the acceptor molecule (Fig. S2, ESI†). Thus estimated alignment of the lowest excited states is summarized in Fig. 2E, and will be further used for the discussion of photophysical properties.

PL decays and rates of photophysical processes

The analysis of time-resolved emission spectra and PL decay curves evidences that all emitters dispersed in the CBP host exhibit TADF (Fig. 2F and Fig. S3A–D, ESI†). In the region of prompt fluorescence (PF), **H** and emitters with bromines in the side rings of the DTA donor (**1Br** and **2Br**) fluoresce with a similar lifetime τ_{PF} close to 15 ns (Table 2). The k_r values seem to depend on the doping ratio more than on the bromine contamination. At 6% and 10% doping with **1Br**, k_r slightly decrease and increase, respectively, by around 15%. In the case of **2Br** in 6% films, k_r decreases twice, but at a higher doping ratio, k_r is only 20% lower as compared to **H**. In **3Br**, PF lifetime increases to 27 ns, which is mainly caused by an almost fivefold k_r decrease. **2Br** and **3Br** exhibit a *ca.* twice faster ISC rate than the rest of the emitters. This is the result of the energetic closeness of the ^{1}CT and ^{3}LE states (Fig. 2E), as the latter state plays an important role in ISC as was revealed previously.[23,30]

As compared to **H**, the delayed fluorescence lifetime (τ_{DF}) of **1Br** and **3Br** shortens *ca.* 1.5-fold. This indicates that the presence of one and/or three heavy atoms in the TDA donor helps to convert triplet excitons to light more than 1.5 times faster. This becomes possible because of 2 and 8 times faster rISC, respectively, as for 6% CBP films. Importantly, in **3Br**, rISC enhancement outranges the decrease of the k_r value.

Surprisingly, the τ_{DF} value of **2Br** is higher than that of **H**, because of the more efficient enhancement of ISC than rISC. As compared to **1Br**, the introduction of a second Br atom has either negligible (6% doping) or even negative (10% doping) effects on the rISC rate (Fig. S4 (ESI†), Table 2). Apparently, in the investigated emitters, the HA-effect is not additive by the number of bromines, hence their relative position should play an important role. Such a peculiar rISC behavior is further explained with the help of quantum chemical calculations.

From the point of view of the geometry–property relationship, it is interesting to compare **3Br** with **Ph-DMAC** (Fig. 1, Fig. S1E and F, ESI†). Due to the large size of three bromine atoms, the donor fragment of **3Br** can have a more twisted structure than **1Br** and **2Br**, but a less rigid one than 9,9-dimethylacridan in **Ph-DMAC**. Under the same conditions, as compared to **Ph-DMAC**, **3Br** exhibits an almost 1.5-fold higher k_r value and a

Table 2 Spectral and photophysical parameters in CBP films

	$w_{X/CBP}$ (%)	PLQY [%]	λ_{PL} [nm]	λ_{Ph} [nm]	ΔE_{ST} [eV]	τ_{PF} [ns]	τ_{DF} [μs]	k_r [10^7] s^{-1}	k_{ISC} [10^7] s^{-1}	k_{rISC} [10^4] s^{-1}
H	6	83	692	706	0.04	16.7	646	3.2	2.1	0.25
	10	51	704	709	0.03	18.8	356	2.7	2.0	0.50
1Br	6	76	665	684	0.08	15.5	422	2.6	3.0	0.48
	10	77	671	690	0.06	15.2	296	2.9	2.9	0.60
2Br	6	98	641	669	0.13	14.8	781	1.6	5.5	0.50
	10	97	647	672	0.10	15.0	442	2.1	3.9	0.50
3Br	6	61	602	648	0.20	27.2	403	0.51	5.0	1.9
	10	71	606	633	0.19	23.3	267	0.58	3.5	2.0
Ph-DMAC	6	71	600	601	0.09	39.4	272	0.39	2.0	1.7

 This journal is © The Royal Society of Chemistry 2022

Open Access Article. Published on 01 August 2022. Downloaded on 2/7/2026 9:48:07 AM.
This article is licensed under a Creative Commons Attribution 3.0 Unported Licence.

slightly faster rISC rate, whilst ΔE_{ST} is more than twice higher. Taking into account the exponential dependence of k_{rISC} on $-\Delta E_{ST}$ from the Marcus–Hush formula (eqn (S1), ESI†) this indicates *ca.* a hundred times higher SOC in **3Br**. This is an important conclusion for further design of **3Br** analogues with lower ΔE_{ST} towards fast rISC emitters.

Rotational isomerism and calculations of the rISC rates

Due to the large size of bromine at the *ortho* positions of benzene rings in the DTA donor, rotations of these rings have increased the energy barrier. This leads to various rotational isomers which can coexist at room temperature in a medium of low viscosity. In amorphous films, which are the media of interest for OLED emitters, high viscosity disables the rotations of large molecular fragments and thus such rotational isomers become individual photophysical species with restricted donor fragment geometries. In the investigated emitters there are three types of dihedral angles which provide rotational isomerism (Fig. 3). First is the dihedral angle θ_L between the plane of the dibenzo[*a*,*c*]phenazine acceptor and linker phenyl ring. In all the investigated rotamers, the optimal value θ_L is near +35° or −35° (Table 3), where the sign defines whether the donor fragment is above or beyond the acceptor plane (relatively to the molecular orientation depicted in Fig. 3). Two next dihedral angles between the linker phenyl ring and side rings A and B are depicted as θ_A and θ_B, respectively.

Due to a large number of structural and electronic parameters, and very poor knowledge of the mechanism of their influence on spin–flip transitions, geometry optimizations and calculations of excited state properties were performed for all possible rotamers. The analysis of electronic properties included radiative deactivation ^{1}CT–S$_0$ and the parameters of ^{3}CT→^{1}CT transition: SOC constants, ΔE_{ST}, activation energy (E_a), which takes into account the internal reorganization energy, and finally calculation of the ^{3}CT→^{1}CT rate constants ($k_{3CT-1CT}$) using the Marcus–Hush equation ((S1), ESI†). To obtain statistically weighted values of f_{1CT-S0} and $k_{3CT-1CT}$, the respective values of all rotamers were added taking into account the contribution of each rotamer provided by relative energies of rotamers and Boltzmann distribution law (S2) (ESI†). As was reported previously, in donor–acceptor type TADF emitters including their HA-derivatives, the rotational[30]

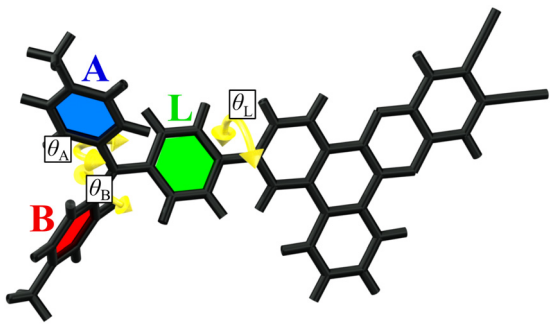

Fig. 3 Structure of the investigated emitters with three types of dihedral angles (θ_A, θ_B and θ_L) highlighted which provide rotational isomerism.

Table 3 Calculated geometry and electronic parameters of the key rotamers

	Unit	H-1	H-2	1Br-exo	1Br-endo	2Br-syn	2Br-anti	3Br-c3V	3Br-A	3Br-B	3Br-C
θ_L	[°]	27.9	−28.8	−23.1	−22.5	17.8	17.6	19.0	19.5	17.8	18.1
θ_A	[°]	−64.6	−65.1	−69.1	−74.9	−63.5	−68.5	76.6	76.5	−77.5	−71.0
θ_B	[°]	−64.8	−65.2	55.3	−74.9	77.3	−68.4	−78.0	61.7	−73.6	61.4
$\Delta G(S_1)$	[a.u.]	−1889.647927	−1889.647680	−1902.208629	−1902.206972	−1914.764446	−1914.765059	−1927.32269	−1927.324124	−1927.322466	−1927.321232
$\Delta G(T_1)$	[a.u.]	−1889.650547	−1889.649878	−1902.211800	−1902.211480	−1914.773697	−1914.774187	−1927.33009	−1927.328483	−1927.330665	−1927.331147
S_1–S_0	[eV]	1.38	1.37	1.58	1.59	1.74	1.77	1.84	1.77	1.85	1.80
S_1–S_0	[nm]	899	907	787	779	713	702	674	702	670	687
f_{CT-S0}		0.228	0.209	0.331	0.335	0.438	0.461	0.407	0.340	0.450	0.39
T_1–S_0	[eV]	1.26	1.26	1.38	1.38	1.45	1.43	1.55	1.55	1.53	1.54
T_1–S_0	[nm]	980	984	896	892	854	864	797	800	810	805
T_2–S_0	[eV]	1.92	1.91	1.96	1.96	2.01	2.03	2.00	1.96	2.02	1.99
T_2–S_0	[nm]	645	646	632	631	616	610	619	630	613	622
SOC_{T1-S1}	[cm^{-1}]	0.06	0.08	0.32	0.44	0.58	0.04	0.58	0.88	2.3	3.45
SOC_{T2-S1}	[cm^{-1}]	0.23	0.17	0.58	0.74	0.40	0.13	0.39	0.65	0.87	3.08
$\Delta E_{3CT-1CT}$	[eV]	0.03	0.03	0.11	0.12	0.10	0.15	0.20	0.14	0.24	0.18
$\lambda_{3CT-1CT}$	[eV]	0.34	0.33	0.38	0.38	0.39	0.39	0.41	0.41	0.41	0.41
E_a	[eV]	0.18	0.17	0.23	0.23	0.23	0.25	0.29	0.25	0.32	0.28
$k_{3CT-1CT}\cdot\chi_{3CT}$	[10^4 s^{-1}]	0.16	0.30	0.56	0.80	1.8	2.8×10^{-3}	0.14	1.54	0.93	8.0
$k_{3LE-1CT}\cdot\chi_{3LE}$	[10^4 s^{-1}]	0.032	9×10^{-3}	1×10^{-3}	1×10^{-3}	1×10^{-3}	1×10^{-3}	$<1 \times 10^{-3}$	$<1 \times 10^{-3}$	$<1 \times 10^{-3}$	3×10^{-3}

θ_L, θ_A, θ_B – dihedral angles between phenyl rings of the donor fragment (Fig. 3). $\Delta G(S_1)$, $\Delta G(T_1)$ – Gibbs free energies of S_1 and T_1 electronic states, respectively. S_1–S_0, T_1–S_0, T_2–S_0 – predicted energies of respective vertical transitions. f_{1CT-S0} – oscillator strength of the S_1–S_0 transition. SOC_{T1-S1}, SOC_{T2-S1} – SOC constants for T_1–S_1 and T_2–S_1 transitions, respectively. $\Delta E_{3CT-1CT}$ – energy gap between ^{3}CT and ^{1}CT states. $\lambda_{3CT-1CT}$ – reorganization energy. E_a – activation energy. χ_{3CT},χ_{3LE} – relative population of ^{3}CT and ^{3}LE states at room temperature predicted by Boltzmann distribution (Section S2, ESI).

Open Access Article. Published on 01 August 2022. Downloaded on 2/7/2026 9:48:07 AM.
This article is licensed under a Creative Commons Attribution 3.0 Unported Licence.

and vibrational[23] isomerism has key importance for efficient rISC *via* the ^{3}CT→^{1}CT pathway.

According to the experimental data, the k_r values show complex behavior depending on the number of bromine atoms and the emitter/CBP doping ratio indicating the specific role of intermolecular interactions in amorphous films (Table 2). Regarding the aim of this study, the important observation is that **H**, **1Br**, and **2Br** show rather similar k_r values in the 2–3 × 10^7 s^{-1} range. Neither statistically weighted calculated $f_{1CT\text{-}S0}$ values (Table 1) nor $f_{1CT\text{-}S0}$ of individual rotamers (Fig. S5, S6, Table S2, ESI†) show a substantial decrease with the growing number of bromines in the emitter.

The statistically weighted $k_{3CT-1CT}$ correlate very well with the experimental k_{rISC} values (Fig. 4), which confirms that various rotamers are responsible for the photophysical behavior of emitters in films. This also enables the analysis of ^{3}CT→^{1}CT transition parameters in key rotamers as discussed below. We should note that the contribution of the second triplet state in rISC was found to be negligible even in **3Br**, where the ^{3}LE-state is relatively close to the ^{3}CT one (Fig. 2E). The statistically weighted $k_{3LE-1CT}$ values do not exceed 1 × 10^3 s^{-1}, which is only 5% of the $k_{3CT-1CT}$ one (Fig. 4 and Section S2, ESI†). In other compounds, the ^{3}LE→^{1}CT transition is slower. One can conclude that such a slow rISC pathway can only compete in rotamers with the slowest ^{3}CT→^{1}CT transition such as **2Br**-*anti* ones (Table 3), but even in the latter case, $k_{3LE-1CT}$ is three times lower than $k_{3CT-1CT}$.

In **H**, two rotamers with different θ_L (**H-1** and **H-2** in Table 3, Table S2, Fig. S5 and S7, ESI†) have different SOC constants: 0.06 and 0.08 cm^{-1}, in spite of the absence of HAs and minor differences in the electronic parameters including ΔE_{ST} and E_a (Fig. S5, ESI†). Different positions of linker phenyl provide different orientations of donor *versus* acceptor; in the rotamer **H-2** with θ_L = –29°, the donor fragment is more twisted *versus* the acceptor, providing larger change in the orbital moment ΔL during the ^{3}CT→^{1}CT transition (Fig. S7, ESI†). One should note that the change of orbital moment is typically small as for transition between states of very close nature. In spite of minor changes in ΔL and SOC, the calculated $k_{3CT-1CT}$ values of **H** rotamers differ by 2 times.

In **1Br**, the highly asymmetric donor fragment enables 16 rotamers. The calculated $f_{1CT\text{-}S0}$ values are very similar for all rotamers (Fig. S5, ESI†). As compared to **H**, the calculated ΔE_{ST} values are increased more than 3 times, and for all rotamers of **1Br** they exceed 100 meV. The presence of a heavy atom causes more than a fivefold SOC constant rise up to 0.31–0.45 cm^{-1}, depending on the rotamer structure. The highest SOC is observed when the bromine atom in the donor fragment is oriented towards the acceptor (8 rotamers are attributed to **1Br**-*endo* group in Fig. 5 and Fig. S5, ESI†), whilst the opposite direction provides the lowest value (8 rotamers, **1Br**-*exo*). SOC rise is, however, partially compensated by the ΔE_{ST} increase, which provides more than 3 times rISC acceleration as compared to **H**. As neither experimental k_r nor calculated $f_{1CT\text{-}S0}$ values of **1Br** are substantially lower than those of **H**, one can conclude that the introduction of one bromine atom has a positive effect on triplet harvesting in such emitters.

Regarding the relative position of two bromine atoms, 16 rotamers of **2Br** can be divided into two main groups: *syn* and *anti*. The expected strong heavy-atom effect is realized only in the *syn* rotamers with both bromines on the same side of the acceptor plane (Fig. 5 and Fig. S5 (ESI†), Table 3). In such HA configurations, the increased SOC constants reach 0.60 cm^{-1}. In the *anti* rotamers, bromines on the different sides of the acceptor plane cause surprisingly low SOC constants, dropping below 0.05 cm^{-1}, resembling those for an HA-free emitter **H**. In the result, the $k_{3CT-1CT}$ of the most efficient *syn* rotamer is 650 higher than that of the least efficient *anti* one. These observations indicate that the HA effect can be zeroed when heavy atoms are situated in a symmetric way or at the opposite sides of the donor fragment.

3Br exhibits the most complex isomerism. Regarding the relative position of three bromine atoms, its 32 rotamers can be divided into four groups. The rotamers in which bromines and the nitrogen atom form a symmetric pyramid-like structure of C_{3V} symmetry (**3Br-c$_{3v}$** in Fig. 5) exhibit the lowest SOC values below 0.70 cm^{-1} (Fig. S6 (ESI†), Table 3 and Table S2, ESI†). When such a symmetry is broken by the rotation of A or B rings so that side bromines occur in the *anti* configuration (**3Br**-A on Fig. 5 and Fig. S6, ESI†), the SOC increases slightly up to 0.9 cm^{-1}. As an exception, another group of *anti* rotamers with bromine atoms of the side rings oriented towards the acceptor fragment exhibit a high SOC reaching 2.40 cm^{-1} (**3Br**-B). In such rotamers, in contrast to *anti* rotamers of **2Br**, the symmetry of the *anti* configuration is broken by the bromine in the linker phenyl of **3Br**. The most impressive SOC values reaching 3.50 cm^{-1} are observed in the case when the C_{3V} symmetry is broken *via* rotation of the linker phenyl ring, so that bromines in the side phenyl rings remain in the *syn* configuration (**3Br**-C). Such a dependence on the relative positions of bromine atoms supports the conclusion that the asymmetric configuration of HAs favors the maximal increase of SOC. From the point of view of rISC efficiency, a negative factor of all **3Br** rotamers is high ΔE_{ST} which ranges from 140 to 240 meV. Remarkably, in spite of such a high ΔE_{ST} value of 180 meV, high SOC in the most efficient rotamers **3Br**-C enables $k_{3CT-1CT}$ above 8 × 10^4 s^{-1} outranging more than 25 times that in **H**.

The increase of SOC within an isolated atom or molecular system is usually explained by the increase of the orbital and/or spin transition moment, because these two quantum values define the change of the total angular momentum and thus the spin–orbit coupling.[6] Thorough analysis of electronic parameters led us to the conclusion that, regarding total angular momentum, the ^{3}CT→^{1}CT transition in various rotamers bearing heavy atom(s) remains very similar. None of the calculated electronic parameters by itself can explain the drastic change of SOC and rISC rates. Neither calculated changes in the NTO orbitals of ^{3}CT→^{1}CT transitions nor partial contributions of electronic densities on the bromine atom below (Fig. S8 and S9, ESI†) reveal a substantial change in the orbital transition moment. Triplet spin density distribution (TSDD, Fig. S10, ESI†)

 This journal is © The Royal Society of Chemistry 2022

Open Access Article. Published on 01 August 2022. Downloaded on 2/7/2026 9:48:07 AM.
This article is licensed under a Creative Commons Attribution 3.0 Unported Licence.

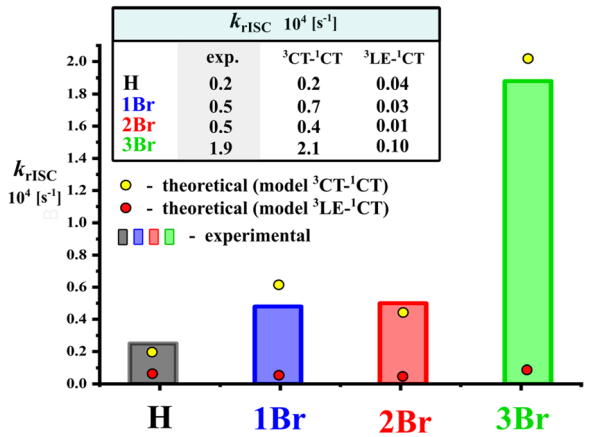

Fig. 4 Comparison of experimental k_{rISC} with calculated statistically weighted $k_{3CT-1CT}$ and $k_{3LE-1CT}$.

maps remain similar and the contribution of bromine atom(s) is negligible too, which indicates that the change of spin transition moment is very similar for all isomers. Therefore, the observed heavy-atom effect cannot be regarded as the internal one. On the other hand, the notion "external heavy-atom effect" cannot be applied either, as heavy atoms are covalently bonded to the chromophore fragment.

In spite of the absence of direct influence of heavy atom(s) on the electronic spin–flip transition, their presence and orientation change immensely the SOC matrix elements and thus the direction and value of total angular momentum. The observed phenomenon can be regarded as the heavy-atom field effect (HAFE). Such a field interacts with the electron density during the electronic transition enhancing the change of spin. The peculiarity of the observed HAFE phenomenon, namely the inactivity of HAs in either ^{1}CT-S_0 or ^{3}CT→^{1}CT transitions as one can conclude on the basis of NTO analysis (Fig. S8, ESI†) can be explained by the electron-withdrawing effect of bromine which disables its participation in the charge-transfer transition in the role of the donor.

Most likely, the HAFE has a direction defined by the orientation of heavy atoms. In fact, the analysis of the SOC matrix elements within the geometry coordinates of each rotamer (Fig. 5) indicates that maximal strengths of the HAFE and thus the highest SOC are achieved in two cases. The first one with the most substantial growth of SOC matrix elements is observed when HAs' relative alignment is asymmetrical (compare **3Br-c_{3v}** and other rotamers of **3Br**, Fig. 5) and the field of one heavy atom cannot be compensated by another one (compare *syn* and *anti* **2Br** rotamers). The second case is when heavy atoms are orientated towards the change of electronic density during the ^{3}CT→^{1}CT transition (compare *endo* with *exo* **1Br** rotamers, and **2Br**-*syn* with **2Br**-*anti*, Fig. 5). In fact, the symmetric orientation of bromines in **3Br-C_{3V}** and especially **2Br**-*anti* rotamers results in self-compensation or even zeroing of the HA effect.

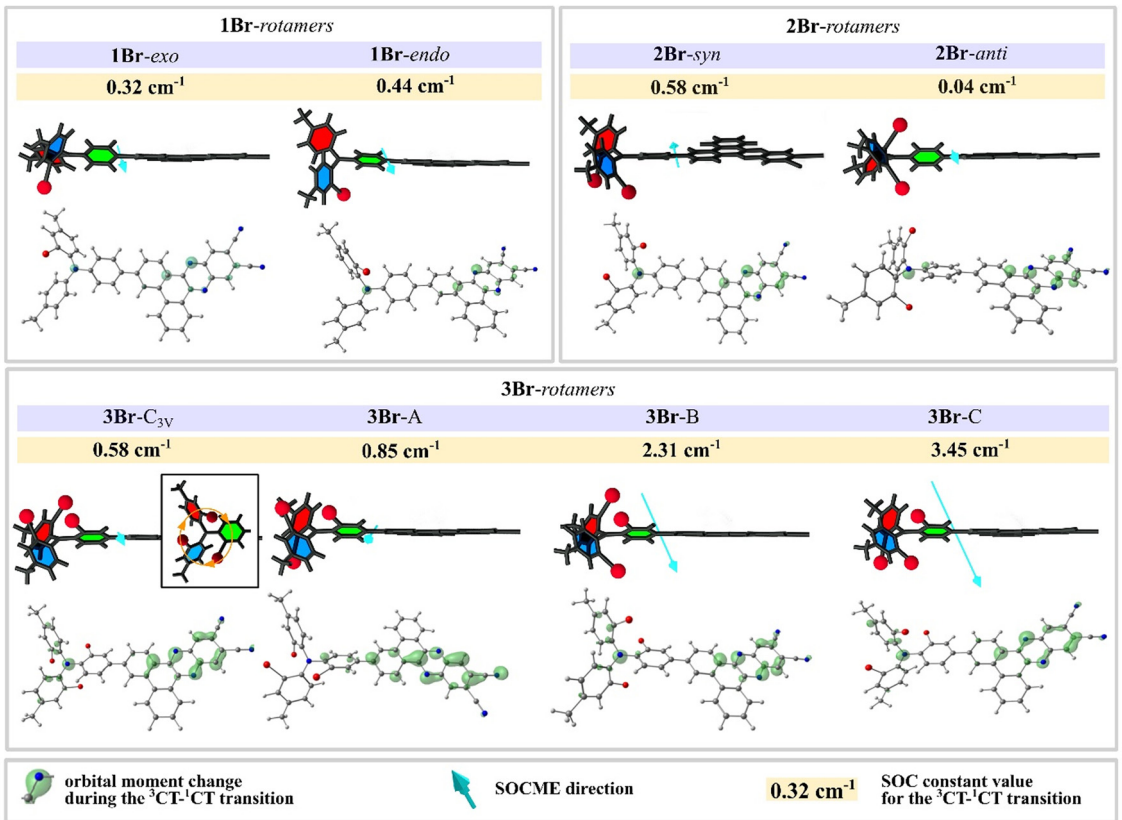

Fig. 5 Optimized structures of key rotamers (see Fig. S5 and S6, ESI†) of **1Br**, **2Br**, and **3Br** with SOCME value, SOCME direction (turquoise arrows), and ΔL (green clouds, contour value 0.02); illustrations show the simplified orientation of heavy atoms relative to the acceptor plane.

Open Access Article. Published on 01 August 2022. Downloaded on 2/7/2026 9:48:07 AM.
This article is licensed under a Creative Commons Attribution 3.0 Unported Licence.

To the best of our knowledge, neither observation of the HAFE nor the possibility of self-compensation of the HA effect was reported before. The latter peculiarity is not intuitive for materials with more than one HA, and can lead to an imaginary lack of the HA effect or even the opposite result of SOC decrease. The possibility of formation of rotamers with zero HAFE during synthesis or sample preparation evidences another challenge for hybrid material engineers to analyze and eliminate such species at the stage of molecular design planning to achieve efficient rISC.

Conclusions

The results of the above discussed experimental and computational investigations evidence that hybrid organic materials bearing abundant heavy atoms in fact can solve the dilemma of all-organic TADF materials given by eqn 1. In the investigated example, selective acceleration of the ^{3}CT→^{1}CT rISC pathway without a drastic decrease of the S_1–S_0 oscillator strength is possible in a partially conjugated D–A type emitter, when heavy atoms do not self-compensate the created field and are oriented towards the fragment transition orbital moment. The most representative examples are various rotamers of **2Br** and **3Br** with similar oscillator strength values but very different SOC and rISC rates (Fig. S5 and S6, ESI†). This is a clear evidence that in contrast to pure organic emitters such hybrid molecular systems disobey the inverse relationship of $f_{1CT\text{-}S0}$ and k_{rISC}. This is supported by the following:

(1) the $f_{1CT\text{-}S0}$ values measured for absorption as well as calculated ones, which indicate that bromine in the role of a heavy atom does not decrease the rate of radiative deactivation *via* S_1–S_0 transition;

(2) photophysical features of **1Br** in 10% ww. film, which in comparison to **H** has twice higher k_{rISC} and only 1.2 times smaller k_r;

(3) different rotamers of **2Br** and **3Br**, which have extremely different k_{rISC} rates, but close $f_{1CT\text{-}S0}$ ones.

On the one hand, the applied bromine is a good choice for the role of a heavy atom as it can be easily introduced by common and powerful synthetic methods. However, its pronounced electron-withdrawing influence on the donor fragment reduces the charge-transfer strength leading to the blue-shift of TADF and increase of ΔE_{ST}. Both these factors are undesired for red emitters, whilst the latter one is negative for all TADF materials in general. Nevertheless, thanks to high SOC, in **3Br** with a 200 meV energy gap almost disabling TADF, the rISC rate is the highest one. Another negative factor of the increase of ^{1}CT energy especially in **2Br** and **3Br** is the decrease of the ^{1}CT→^{3}LE energy gap. This leads to the acceleration of ISC, and thus faster conversion of singlet states to triplet ones.

The analysis of various rotational isomers of the investigated emitters evidences that further improvement of hybrid organic emitters with the HAFE can be probably achieved *via* the stereoselective control of the position of HAs in the molecular structure. In the example of **3Br**, selective synthesis or isolation of **3Br-C** rotamers could provide a further fourfold rISC enhancement without the decrease of the fluorescence rate, making such an emitter more attractive commercially.

Conflicts of interest

There are no conflicts to declare.

Acknowledgements

Financial support within the LIDER XI grant LIDER/47/0190/L-11/19/NCBR/2020 (M. M., D. G., E. H., K. K., and I. E. S) and CHEMFIZ program WND-POWR.03.02.00-00-I059/16 (M. M.) of National Centre for Research and Development (NCBR), Poland is gratefully acknowledged. Quantum chemical calculations were performed on the computers of the Wroclaw Centre for Networking and Supercomputing (WCSS), Poland.

References

1 S. H. Mir, L. A. Nagahara, T. Thundat, P. Mokarian-Tabari, H. Furukawa and A. Khosla, *J. Electrochem. Soc.*, 2018, **165**, 3137–3156.
2 V. Trifiletti, C. Asker, G. Tseberlidis, S. Riva, K. Zhao, W. Tang, S. Binetti and O. Fenwic, *Front. Electron.*, 2021, **2**, 758603.
3 T. Hua, L. Zhan, N. Li, Z. Huang, X. Cao, Z. Xiao, S. Gong, C. Zhou, C. Zhong and C. Yang, *Chem. Eng. J.*, 2021, **426**, 131169.
4 Y. Xiang, Y. Zhao, N. Xu, S. Gong, F. Ni, K. Wu, J. Luo, G. Xie, Z.-H. Lu and C. Yang, *J. Mater. Chem. C*, 2017, **5**, 12204–12210.
5 E. Longhi and L. De Cola, *Iridium(III) Complexes for OLED Application, Iridium(III) in Optoelectronic and Photonics Applications*, John Wiley & Sons, Ltd, Chichester, UK, 2017, p. 205.
6 W. Shao, H. Jiang, R. Ansari, P. M. Zimmerman and J. Kim, *Chem. Sci.*, 2022, **13**, 789–797.
7 M. Godumala, A. V. Kumar and R. Chandrasekar, *J. Mater. Chem. C*, 2021, **9**, 14115–14132.
8 H. F. Higginbotham, M. Okazaki, P. de Silva, S. Minakata, Y. Takeda and P. Data, *ACS Appl. Mater. Interfaces*, 2021, **13**, 2899–2907.
9 D. Lee, O. Bolton, B. C. Kim, J. H. Youk, S. Takayama and J. Kim, *J. Am. Chem. Soc.*, 2013, **135**, 6325–6329.
10 A. Lv, W. Ye, X. Jiang, N. Gan, H. Shi, W. Yao, H. Ma, Z. An and W. Huang, *J. Phys. Chem. Lett.*, 2019, **10**, 1037–1042.
11 Z.-Y. Zhang, Y. Chen and Y. Liu, *Angew. Chem., Int. Ed.*, 2019, **58**, 6028–6032.
12 H. Uoyama, K. Goushi, K. Shizu, H. Nomura and C. Adachi, *Nature*, 2012, **492**, 234–238.
13 X. Yin, Y. He, X. Wang, Z. Wu, E. Pang, J. Xu and J. Wang, *Front. Chem.*, 2020, **8**, 725.
14 T. Huang, X. Song, M. Cai, D. Zhang and L. Duan, *Mater. Today Energy*, 2021, **21**, 100705.

 This journal is © The Royal Society of Chemistry 2022

Open Access Article. Published on 01 August 2022. Downloaded on 2/7/2026 9:48:07 AM.
This article is licensed under a Creative Commons Attribution 3.0 Unported Licence.

15 Y. Ren, Y. Wada, K. Suzuki, Y. Kusakabe, J. Geldsetzer and H. Kaji, *Appl. Phys. Express*, 2021, **14**, 071003.
16 D. Song, Y. Yu, L. Yue, D. Zhong, Y. Zhang, X. Yang, Y. Sun, G. Zhou and Z. Wu, *J. Mater. Chem. C*, 2019, **7**, 11953.
17 T. Hua, L. Zhan, N. Li, Z. Huang, X. Cao, Z. Xiao, S. Gong, C. Zhou, C. Zhong and C. Yang, *Chem. Eng. Sci.*, 2021, **426**, 131169.
18 K. Masui, H. Nakanotani and C. Adachi, *Org. Electron.*, 2013, **14**, 2721–2726.
19 Y. Zhang and S. R. Forrest, *Phys. Rev. Lett.*, 2012, **108**, 267404.
20 R. Furue, K. Matsuo, Y. Ashikari, H. Ooka, N. Amanokura and T. Yasuda, *Adv. Opt. Mater.*, 2018, **6**, 1701147.
21 Y.-L. Zhang, Q. Ran, Q. Wang, Y. Liu, C. Hanisch, S. Reineke, J. Fan and L.-S. Liao, *Adv. Mater.*, 2019, **31**, 1902368.
22 J. H. Kim, J. H. Yun and J. Y. Lee, *Adv. Opt. Mater.*, 2018, **6**, 1800255.
23 M. Mońka, I. E. Serdiuk, K. Kozakiewicz, E. Hoffman, J. Szumilas, A. Kubicki, S. Y. Park and P. Bojarski, *J. Mater. Chem. C*, 2022, **10**, 7925–7934.
24 R. D. Burkhart and N. I. John, *J. Phys. Chem.*, 1991, **95**, 7189–7196.
25 U. Balijapalli, Y.-T. Lee, B. S. B. Karunathilaka, G. Tumen-Ulzii, M. Auffray, Y. Tsuchiya, H. Nakanotani and C. Adachi, *Angew. Chem., Int. Ed.*, 2021, **60**, 19364–19373.
26 A. A. Kubicki, P. Bojarski, M. Grinberg, M. Sadownik and B. Kukliński, *Opt. Commun.*, 2006, **269**, 275–280.
27 M. J. Frisch, G. W. Trucks, H. B. Schlegel, G. E. Scuseria, M. A. Robb, J. R. Cheeseman, G. Scalmani, V. Barone, G. A. Petersson and H. Nakatsuji, *et al.*, *Gaussian 16, Revision C.01*, Gaussian, Inc., Wallingford, CT, 2016.
28 A. D. Becke, *J. Chem. Phys.*, 1993, **98**, 1372–1377.
29 F. Neese, *Wiley Interdiscip. Rev.: Comput. Mol. Sci.*, 2012, **2**, 73–78.
30 I. E. Serdiuk, M. Mońka, K. Kozakiewicz, B. Liberek, P. Bojarski and S. Y. Park, *J. Phys. Chem. B*, 2021, **125**, 2696–2706.